Supplement of

Groundwater Maintains Lake Clusters: Groundwater pattern of the Songnen Basin from a Multi-source Remote Sensing Perspective

Xiangmei Liu[1,2], Peng Shen[3], Jiaqi Chen[1*], David Andrew Barry[4], Christian Massari[5], Jiansheng Chen[6], Mingming Feng[7,8], Xi Zhang[9], Fenyan Ma[10], Fei Yang[11], Haixia Jin[1]

[1]*College of Information Science and Engineering, Hohai University, Changzhou 213200, China*
[2]*College of Artificial Intelligence and Automatio, Hohai University, Changzhou, 213200, China*
[3]*Shanghai Aerospace Electronics Co., Ltd., Shanghai, 201821, China*
[4]*Ecological Engineering Laboratory, Environmental Engineering Institute, Faculty of Architecture, Civil and Environmental Engineering, École Polytechnique Fédérale de Lausanne, Lausanne 1015, Switzerland*
[5]*National Research Council (CNR), Research Institute for Geo-Hydrological Protection, Perugia, 06126, Italy*
[6]*School of Earth Science and Engineering, Hohai University, Nanjing 211100, China*
[7]*Key Laboratory of Wetland Ecology and Environment, Northeast Institute of Geography and Agroecology, Chinese Academy of Sciences, Changchun 130102, China*
[8]*University of Chinese Academy of Sciences, Beijing 100049, China*
[9]*Institute of Hydrogeology and Environmental Geology, Chinese Academy of Geological Sciences, Xiamen, 361000, China*
[10]*College of Energy and Power Engineering, Lanzhou University of Technology, Lanzhou, 730050, China*
[11]*Hanggin Banner River and Lake Protection Center, Ordos, 017400, China*

[*]Corresponding author: Jiaqi Chen
Email: jiaqichen@hhu.edu.cn

Table of contents:

Figures

Tables

Technical Specifications

Figures:

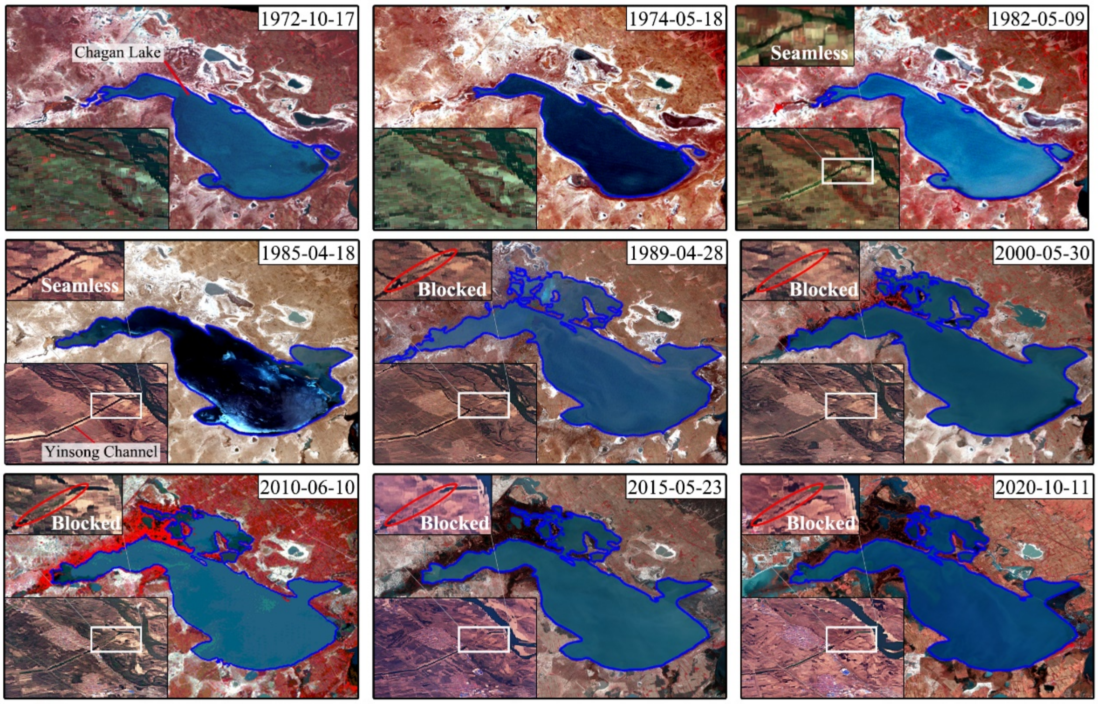

Fig. S1 Results of Chagan Lake area extraction and Yinsong Channel change. The results achieve an overall accuracy of 94.7% with a Kappa coefficient of 0.917, indicating strong agreement between the classified data and reference data.

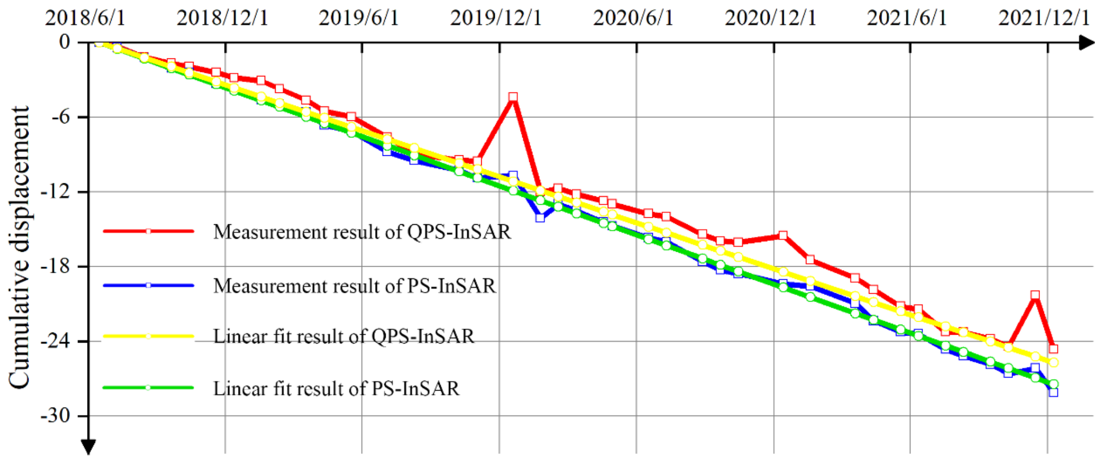

Fig. S2 Deformation measurement results for Songyuan region by PS-InSAR and QPS-InSAR.

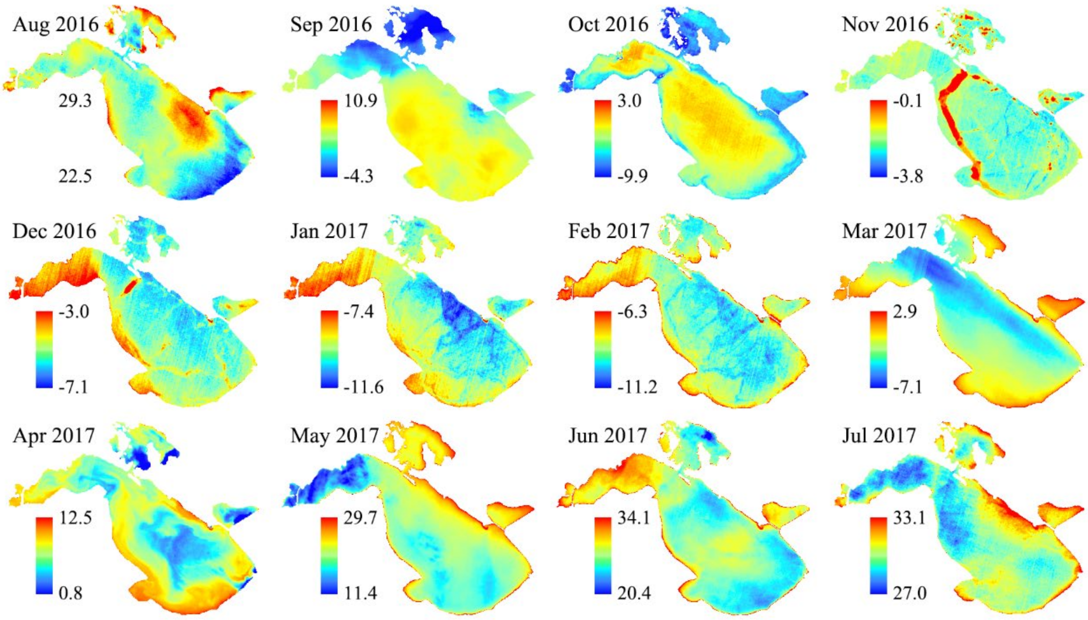

Fig. S3 Water temperature retrieval results of Chagan Lake in 2016-2017. Images were minimally affected by clouds, allowing for a complete depiction of the 12-month temperature variations during this period

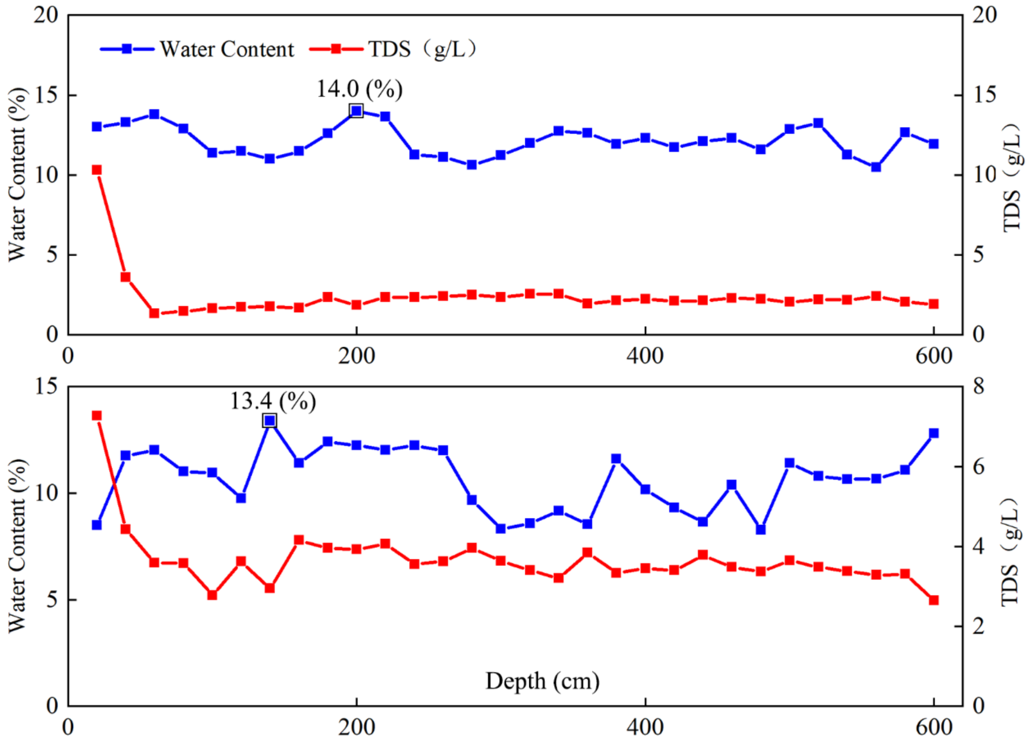

Fig. S4 Soil water content and TDS variation in the Dabaosu Profile.

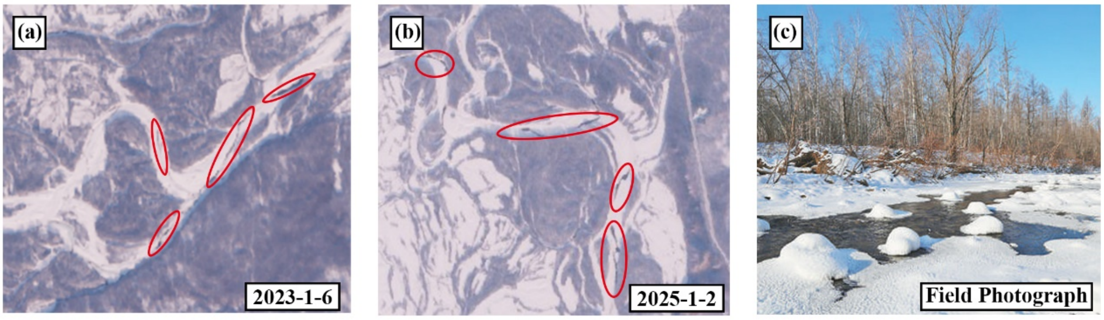

Fig. S5 Images of unfrozen rivers in the Huma River Basin. (a)-(b) Sentinel-2 satellite imagery. Areas circled in red indicate unfrozen zones. (c) Field photograph of the Huzhong area in the Huma River Basin, published by Peoples Daily in January 2023 (https://paper.people.com.cn /rmrb/html/2023-01/17/nw.D110000renmrb_20230117_3-14.htm).

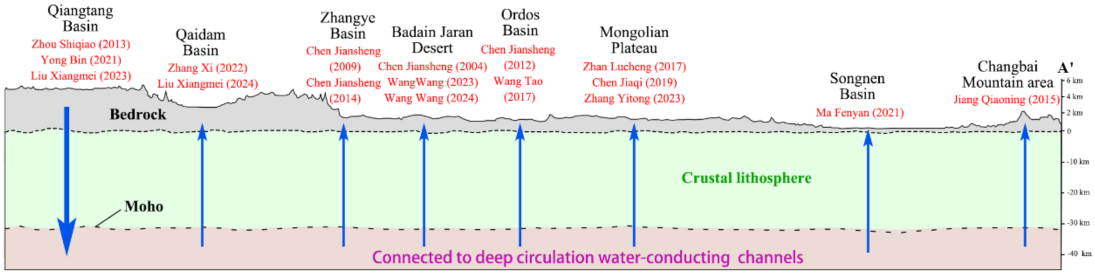

Fig. S6 Deep circulation groundwater recharge path from the Qiangtang Basin moving from west to east and related research literature(Chen et al., 2014; Chen et al., 2019; Chen et al., 2012; Chen et al., 2004; Chen and Wang, 2009; Jiang and Chen, 2015; Liu et al., 2023; Liu et al., 2024; Ma et al., 2021; Wang et al., 2017; Wang et al., 2023; Wang et al., 2024; Yong et al., 2021; Zhan et al., 2017; Zhang et al., 2022; Zhang et al., 2023; Zhou et al., 2013).

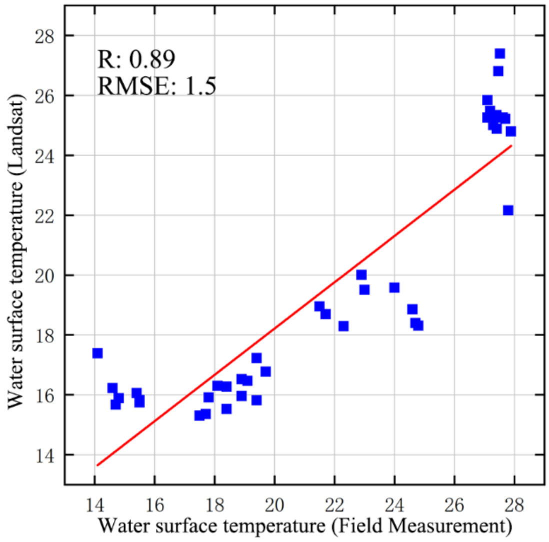

Fig. S7 Landsat water temperature retrieval and validation with ground measurements.

Tables

Table. S1 Description of data used in the study

Data set		Available time	Temporal resolution	Spatial resolution
Sentinel-1A SAR		2014-present	6 days	5m*20m
Landsat	5 Thematic Mapper	1982-2011	16 days	30m*30m
	8 Operational Land Imager	2013-present		
Modis	MOD11A1	2000-present	every day	1 km
	MOD09GA			0.5 km

Table S2 39 interferometric images from June 16, 2018, to December 9, 2021.

Data	Polarization	baseline（m）	Doppler centroid	Time interval（Day）
20180616	VV	3	-0.04	-504
20180710	VV	-24	-0.02	-480
20180815	VV	13	-0.03	-444
20180920	VV	23	0.01	-408
20181014	VV	-50	0.03	-384
20181119	VV	-71	0.02	-348
20181213	VV	13	0	-324
20190118	VV	-52	0.02	-288
20190211	VV	17	-0.02	-264
20190319	VV	-45	-0.02	-228
20190412	VV	6	-0.03	-204
20190518	VV	-117	-0.02	-168
20190705	VV	-56	-0.04	-120
20190810	VV	-20	0	-84
20191009	VV	18	0.01	-24
20191102	VV	0	0.01	0
20191220	VV	-27	-0.01	47
20200125	VV	-126	0.03	83
20200218	VV	-33	0.02	107
20200313	VV	-13	-0.03	131
20200418	VV	-65	-0.04	167
20200430	VV	22	-0.05	179
20200617	VV	-63	-0.05	228
20200711	VV	27	-0.02	252
20200828	VV	-48	0	300
20200921	VV	-41	0.01	324
20201015	VV	-33	0	348
20201214	VV	-141	-0.02	408
20210119	VV	27	-0.02	444
20210320	VV	81	0.02	504
20210413	VV	1	-0.02	528
20210519	VV	-18	-0.05	564
20210612	VV	-69	-0.06	588
20210718	VV	22	-0.05	624
20210811	VV	22	-0.04	648
20210916	VV	-5	-0.01	684
20211010	VV	-29	0.03	708
20211115	VV	-82	-0.01	744
20211209	VV	-54	0	768

Technical Specifications

Specifics of IDCSTFN:

IDCSTFN employs an "encoder-fusion-decoder" architecture. This network consists of four main modules: the High Temporal but Low Spatial (HTLS) encoder, Low Temporal but High Spatial (LTHS) encoder, feature fusion, and reconstruction decoder. The HTLS and LTHS modules are used to extract features from MODIS and Landsat images, respectively. The HTLS is composed of convolutional layers and deconvolutional layers. MODIS images pass through two 3×3 convolutional layers to extract features. Then, a deconvolutional layer expands the low-dimensional feature maps to match the size of the Landsat images. The LTHS consists of four convolutional layers and a max-pooling layer. After two convolutional layers, the max-pooling layer downsamples the Landsat image feature maps. This process compresses them to match the size of the MODIS feature maps while retaining essential feature information.

The feature fusion network primarily consists of two parts: feature fusion and attention residuals. First, the cosine similarity of the MODIS image features is calculated and normalized with a size of $80 \times 80 \times 1$. Second, the number of channels is expanded to C_2 to match the size of the input feature maps. At this point, the difference feature map between the reference image and the predicted image is obtained, and the fused feature map is as follows:

$$FL_{t_0} = w_{0k}(FL_{t_k} + FM_{t_k}) + (1 - w_{0k})FM_{t_0} \quad (k \neq 1) \tag{1}$$

where, FL and FM represent the features extracted by the encoder from Landsat and MODIS images, respectively. Since the fused feature map contains several redundant information, SEBlock was embed into ResBlock to form an attention residual module, SE-ResBlock, which adaptively adjusts the weights of each channel. The ResBlock consists of a convolutional layer with a kernel size of 3×3 and a batch normalization layer, with the output from the convolutional layer being processed by the ReLU activation function. SEBlock primarily consists of squeeze and excitation, which are used to obtain the global average vector and to explore the information between different channels, respectively. The fused features are fed to the SE-ResBlock, which dynamically adjusts the weights of each channel, and reduces redundant features in the network.

The reconstruction decoder consists of a deconvolutional layer and two fully connected layers. The deconvolutional layer restores the feature map to the original Landsat image size. The two successive fully connected layers reduce the dimensions of the fused feature map, resulting in a high-resolution fused image. The dataset of IDCSTFN includes 21 Landsat and Modis data pairs.

Specifics of PS-InSAR:

For the Sentinel-1 satellite, PS-InSAR requires N scenes of Single Look Complex images. The i-th image is denoted as $s_i(i = 1, 2, ..., N)$. The phase difference $\Delta\varphi^{i,k}_{H,T,T_0}$ and $\Delta\varphi^{i,k}_{D,T,T_0}$, which are caused by elevation and linear deformation between the target point T and the reference point T_0, can be expressed as:

$$\Delta\varphi^{i,k}_{H,T,T_0} = \frac{4\pi}{\lambda}\frac{1}{R\sin\theta}\Delta h_{T,T_0}B^{i,k}_n \tag{2}$$

$$\Delta\varphi^{i,k}_{D,T,T_0} = \frac{4\pi}{\lambda}\Delta v_{T,T_0}B^{i,k}_t \tag{3}$$

where $\Delta h_{T,T_0}$ represents the elevation difference between T and T_0. $\Delta v_{T,T_0}$ is the difference in deformation rate. $B^{i,k}_n$ and $B^{i,k}_t$ are the spatial and temporal baselines between the i-th and k-th images. The elevation and subsidence rate of the target point can be estimated by maximizing the temporal coherence ε_T:

$$\left\langle \Delta\hat{h}_T, \Delta\hat{v}_T \right\rangle = \arg(\max(|\varepsilon_T|)) \tag{4}$$

where, ε_T represents the coherence factor of the target, which can be obtained from Equation (5):

$$\varepsilon_T = \frac{1}{N}\sum_{i,k} e^{j(\Delta\varphi_T^{j,k} - \Delta\varphi_{H,T}^{j,k} - \Delta\varphi_{D,T}^{j,k})} \tag{5}$$

where, $\Delta\varphi_T^{j,k}$ and $\Delta\varphi_{H,T}^{j,k}$ represent the differential interferometric phase and elevation phase. $\Delta\varphi_{D,T}^{j,k}$ is the phase containing the terrain deformation information, expressed as:

$$\Delta\varphi_{D,T}^{j,k} = \frac{4\pi}{\lambda}(\Delta v_T B_t^{i,k} + Defo_{non-linear}) \tag{6}$$

where $Defo_{non-linear}$ represents the nonlinear deformation included in $\Delta\varphi_{D,T}^{j,k}$. The temporal coherence factor ε_T in the Equation (5) is approximated as the deviation of the phase residual $\hat{\varepsilon}_p \approx e^{-\delta_\varphi^2/2}$. Consequently, the elevation variance $\delta_{\Delta h}^2$ and deformation rate variance $\delta_{\Delta v}^2$ estimated by PS-InSAR are expressed as:

$$\delta_{\Delta h}^2 = \left(\frac{\lambda R \sin\theta}{4\pi}\right)^2 \frac{\delta_\varphi^2}{N\delta_{B_n}^2} \tag{7}$$

$$\delta_{\Delta v}^2 = \left(\frac{\lambda}{4\pi}\right)^2 \frac{\delta_\varphi^2}{N\delta_{B_t}^2} \tag{8}$$

where δ_φ^2 represents the phase deviation. $\delta_{B_n}^2$ and $\delta_{B_t}^2$ correspond to the spatial and temporal baseline deviations.

Specifics of QPS-InSAR：

The PS-InSAR technique has been widely used in interferometric measurements, particularly in urban areas. Since the irrigated farmland is prevalent, permanent scatterer targets such as buildings are sparsely distributed in the Chagan Lake region, which limits the application of PS-InSAR. Based on PS-InSAR, QPS-InSAR adopts a network similar to small baseline subset InSAR and no longer relies on a single image as the master. This topological network maintains temporal continuity in the interferometric sequence and obtains more dispersed spatial baseline $\delta_{B_n}^2$ and temporal baseline $\delta_{B_t}^2$, reducing the $\delta_{\Delta h}^2$ in the Equation (6) and the $\delta_{\Delta v}^2$ in the Equation (7). QPS-InSAR employs spatial filtering to enhance the signal-to-noise ratio of the phase, enabling reliable information extraction from distributed targets. By substituting the coherence estimate $\left|\hat{\gamma}_P^{j,k}\right|$ into the weighting formula, the temporal coherence can be expressed as:

$$\varepsilon_T = \frac{\sum_{i,k}\left|\hat{\gamma}_P^{j,k}\right| e^{j(\Delta\varphi_T^{j,k} - \Delta\varphi_{H,T}^{j,k} - \Delta\varphi_{D,T}^{j,k})}}{\sum_{i,k}\left|\hat{\gamma}_P^{j,k}\right|} \tag{9}$$

References

Chen, J., Liu, X., Sun, X., Su, Z., Yong, B., 2014. The origin of groundwater in Zhangye Basin, northwestern China, using isotopic signature. Hydrogeology Journal 22, 411.

Chen, J., Lv, J., Li, N., Wang, Q., Wang, J., 2019. External groundwater alleviates the degradation of closed lakes in semi-arid regions of China. Remote Sensing 12, 45.

Chen, J., Wang, C.Y., Tan, H., Rao, W., Liu, X., Sun, X., 2012. New lakes in the Taklamakan Desert. Geophysical research letters 39.

Chen, J.S., Li, L., Wang, J.Y., Barry, D., Sheng, X.F., Gu, W.Z., Zhao, X., Chen, L., 2004. Groundwater maintains dune landscape. Nature 432, 459-460.

Chen, J.S., Wang, C.-y., 2009. Rising springs along the Silk Road. Geology 37, 243-246.

Jiang, Q., Chen, J., 2015. Analysis on water balance of deep cycle groundwater supplying Tianchi Lake of Changbai Mountain. Water Resources Protection 31, 7-13.

Liu, X., Chen, J., Chen, J., Jin, H., 2023. Shrinking lakes of rift valley system in southern Tibet: Is it the climate? Science of The Total Environment 858, 160016.

Liu, X., Chen, J., Zhang, Q., Zhang, X., Wei, E., Wang, N., Wang, Q., Wang, J., Chen, J., 2024. Floating on groundwater: Insight of multi-source remote sensing for Qaidam basin. Journal of Environmental Management 365, 121513.

Ma, F., Chen, J., Chen, J., Wang, T., Han, L., Zhang, X., Yan, J., 2021. Evolution of the hydro-ecological environment and its natural and anthropogenic causes during 1985–2019 in the Nenjiang River basin. Science of The Total Environment 799, 149256.

Wang, T., Chen, J., Ge, J., Zhan, L., 2017. Isotopic evidence of allogenic groundwater recharge in the Northern Ordos Basin. Journal of Radioanalytical and Nuclear Chemistry 314, 1595-1606.

Wang, W., Chen, J., Chen, J., Wang, T., Zhan, L., Zhang, Y., Ma, X., 2023. Contribution of groundwater to the formation of sand dunes in the Badain Jaran Desert, China. Journal of Arid Land 15, 1340-1354.

Wang, W., Chen, J., Chen, J., Zhan, L., Wang, T., Zhang, Y., Huang, D., 2024. Basalt and Dune: Critical Factors in Desert Water Resource Development. ACS ES&T Water.

Yong, B., Wang, C.-Y., Chen, J., Chen, J., Barry, D.A., Wang, T., Li, L., 2021. Missing water from the Qiangtang Basin on the Tibetan Plateau. Geology 49, 867-872.

Zhan, L., Chen, J., Xu, Y., Xie, F., Wang, Y., 2017. Allogenic water recharge of groundwater in the Erenhot wasteland of northern China. Journal of Radioanalytical and Nuclear Chemistry 311, 2015-2028.

Zhang, X., Chen, J., Chen, J., Ma, F., Wang, T., 2022. Lake expansion under the Groundwater contribution in Qaidam Basin, China. Remote Sensing 14, 1756.

Zhang, Y., Chen, J., Chen, J., Ma, F., Yan, J., Wang, W., 2023. Characterizing the interaction of groundwater with surface water and precipitation in the Mongolian Plateau in China. Hydrogeology Journal 31, 2323-2336.

Zhou, S., Kang, S., Chen, F., Joswiak, D.R., 2013. Water balance observations reveal significant subsurface water seepage from Lake Nam Co, south-central Tibetan Plateau. Journal of Hydrology 491, 89-99.